Experimental Investigation of the In-Plane Shear Behavior on Needled C/SiC Composites using Digital Image Correlation

G. Yu[1], X. Gao[*1], Y. Song[1, 2]

[1]Jiangsu Province Key Laboratory of Aerospace Power System, Key Laboratory of Aero-engine Thermal Environment and Structure, Ministry of Industry and Information Technology, College of Energy and Power Engineering, Nanjing University of Aeronautics and Astronautics, Nanjing 210016, P.R. China
[2]State Key Laboratory of Mechanics and Control of Mechanical Structures, Nanjing University of Aeronautics and Astronautics, Nanjing 210016, P.R. China

Abstract

In this study, the digital image correlation (DIC) technique was employed as a full-field measuring tool to analyze the in-plane shear deformation behavior of needled C/SiC composites. The non-linear in-plane shear stress-strain curve was obtained. The shear strain distribution and evolution were analyzed. The correlation between the shear strain distribution along the notches and the structure of needled preforms was investigated. The initiation and propagation of the cracks on the surface of shear specimens were studied. The failure mechanisms of needled C/SiC composites under shear loading were also investigated using a scanning electron microscope and an optical camera.

Keywords: Shear behavior, C/SiC composites, digital image correlation, strain field, failure mechanism

I. Introduction

Carbon-fiber-reinforced silicon-carbide-matrix composites (C/SiC composites), which are composed of carbon fiber preforms and SiC matrix, are considered to be one of the most potential candidate materials for elevated-temperature structures on account of their excellent thermal, physical and mechanical performance at room and elevated temperatures [1, 2, 3]. Many forming techniques are available to manufacture fiber preforms of C/SiC composites, such as stitching, weaving, needling, braiding [4], etc. The advantages and disadvantages of these forming techniques have been summarized [4–7]. It has been revealed that the needling technology is an economical and effective preform fabrication technology which is also suitable for producing complex components [8]. The mechanical performance of needled composites is better than that of two-dimensional laminates [5, 9]. Needled C/SiC composites have been widely used in many situations, such as nozzles of solid rocket motors, exit cones, brake systems [10, 11], etc. It is necessary to understand the mechanical behavior and corresponding mechanisms during the design process of these components.

Previous research work has been done to investigate the mechanical behavior of needled C/SiC composites. Li *et al.* [12] investigated the dynamic compressive behavior of needled C/SiC composites at room temperature. Nie *et al.* [13] studied the tensile non-linear behavior of needled C/SiC composites. Han *et al.* [14] studied the flexural characteristics of needled C/SiC composites. Mei *et al.* [15] found that the strengthening features of needled C/SiC composites are caused by the release of thermal residual stress. Xu *et al.* [16] compared the impact of yarn size on tensile and in-plane shear properties of needled C/SiC composites. Fang *et al.* [17] investigated the effect of stress level on the fatigue strengthening behavior of needled C/SiC composites at room temperature. All these previous studies are achievable and helpful in understanding the mechanical behavior of needled C/SiC composites, but the research work on the shear behavior of the material is still insufficient. The shear strain field evolution, shear strain distribution and the failure mechanisms of needled C/SiC composites under shear loading are still poorly understood. Moreover, substantial shear stresses are found around the holes and the notches of these components [18]. The shear failure may be dominant in these components with holes and notches as the shear strength of needled C/SiC composites is smaller than their tensile and compressive strength [19]. To utilize the needled C/SiC composites efficiently and safely, it is critical to have a comprehensive understanding of the in-plane shear behavior of the material.

In this study, the digital image correlation (DIC) technique was employed as a full-field measuring tool to analyze the in-plane shear deformation of needled C/SiC composites. The shear strain field distribution, the shear strain field evolution and the non-linear shear stress-strain curve were analyzed. The shear strain distribution along the notches was studied. The initiation and propagation of the cracks on the surface of shear specimens were observed. The shear failure mechanisms of needled C/SiC composites were also investigated. The main contributions of this paper were the discovery of wave-type shear strain distribution between the notches, the multi-stage evolution analysis of the shear strain field, and the shear failure mechanism of the material.

* Corresponding author: gaoxiguang@nuaa.edu.cn

II. Experimental

(1) Material and specimens

The structure of needled C/SiC composites is illustrated in Fig. 1. The needled fiber preforms were supplied by Tianniao High Technology (Jiangsu, China). The needled fiber preforms were composed of unidirectional non-woven fiber cloths (T700–6K, Toray, Japan) and short-cut fiber felts (T700–12K, Toray, Japan). The needled fiber bundles were introduced through the thickness to keep fiber cloths and felts together. The thickness of short-cut fiber felts was ~ 160 μm. The density of the needled fiber bundles was 10 punch/cm². The unidirectional non-woven fiber cloths were laminated in the orientations of 0° and 90°. As shown in Fig. 1, three 0° fiber cloth layers, two 90° fiber cloth layers and six short-cut fiber felt layers were laminated alternatively in the preforms. The fiber preforms were cut into square plates with a side length of 200 mm. The chemical vapor infiltration (CVI) technique was utilized to densify the needled fiber preforms. A pyrolytic carbon layer was deposited on the surface of the carbon fibers before the densification of the silicon carbide matrices for the purpose of protecting the carbon fibers and weakening the interfacial bonding between the carbon fibers and SiC matrix [20]. Methyltrichlorosilane (MTS, CH_3SiCl_3) was utilized as a precursor [21,22] to deposit the SiC matrix with a rate of 200 g/h. The MTS was carried by hydrogen [22] (H_2, 0.2 m³/h). Argon (Ar, 0.2 m³/h) was used as dilute gas to slow down the reaction rate of the deposition process [22]. The isothermal CVI apparatus was employed to deposit a SiC matrix with a temperature of 1100 °C. The deposition time was approximately 600 h. The fiber volume fraction is ~ 35 % with a porosity of ~ 10 %, and the density of the composites is ~ 2.0 g/cm³.

The Iosipescu double-notch shear specimen and the Iosipescu shear fixture [23] were used to implement the in-plane shear tests of needled C/SiC composites. The shear specimens were cut from a 200 mm × 200 mm × 4.00 mm needled C/SiC composite plate by means of a water-jet cutting machine and the cutting surfaces were polished with a diamond grinder. The 0° fiber bundles of the shear specimen should be oriented along the length direction while the 90° fiber bundles should be oriented along the width direction. The load applied on the Iosipescu shear fixture should be oriented along the width direction of the specimen. The configuration of the shear specimen is illustrated in Fig. 2.

(2) Digital image correlation full-field measurement technique

The digital image correlation (DIC) technique is a simple and robust non-contact optical full-field surface displacement and strain measuring method which was developed in the 1980s. The DIC technique is based on the framework of the pattern recognition between two images (undeformed and deformed) of the specimen covered with random speckle patterns (black and white dots) [24,25,26]. The testing surface (target surface) preparation of the DIC technique is effortless and the cost of the testing equipment is reasonable [27,28]. The basic principle of the DIC technique (shown in Fig. 3) is to calculate and search for
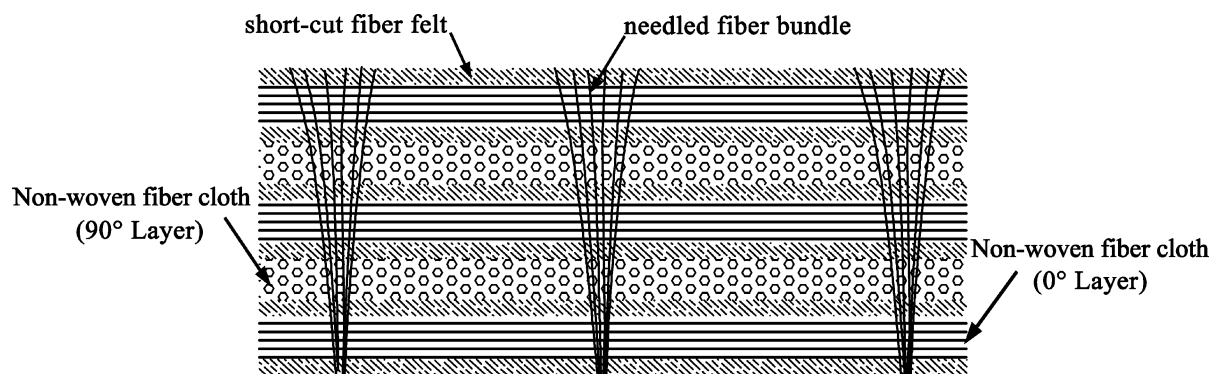

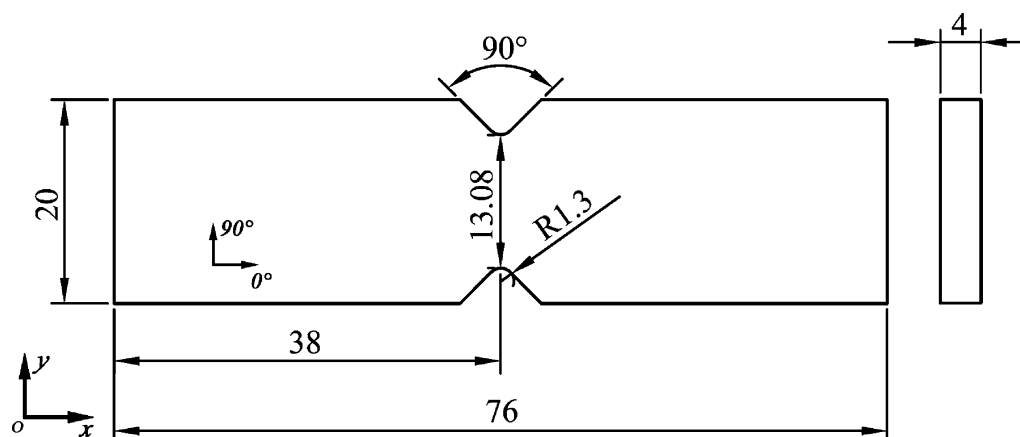**Fig. 1:** Microstructure of needled C/SiC composites.

Fig. 2: Geometry and dimension of the Iosipescu double-notch shear specimen.

the maximum correlation between the identifiable facets of the target surface in the undeformed and deformed state [29,30]. The set of pixels in the identifiable facets is called a subset and determines the region of the target surface being traced. The step denotes the distance between two adjacent subsets. With the help of DIC arithmetic, the displacement field of the target surface can be achieved. During the DIC measuring process, the digital cameras should first be calibrated using a calibration target. After the calibration process, the deformation of the target surface is continuously recorded by cameras. The displacements and strains can be obtained from the recorded images using the DIC post-processing software [31].

(3) Testing details

The typical experimental setup used in the present study consists of a DIC testing system (illustrated in Fig. 4) and an Instron 5982 (100 kN) electronic universal testing machine. The DIC testing system is provided by Correlated Solutions, Inc. Two gigabit Ethernet (GigE) 12-bit charge coupled device (CCD) cameras with a resolution of 4827 pixels × 3248 pixels were used for image collection. A tripod was utilized to adjust the position and maintain stability of the cameras. The inbuilt spirit level on tripod was used to ensure horizontal level. The random sparkle pattern was applied to the shear specimen using acrylic white matte aerosol spray paint (Guangzhou Botny Chemical Co., Ltd) as the black surface of the material. The Iosipescu shear fixture was mounted on the Instron 5982 electronic universal testing machine. The shear specimen was properly aligned and fixed in the Iosipescu shear fixture. Two light-emitting diode light sources were imposed to illuminate the specimen and reduce the influence of environment light change. The relative distance between the shear specimen and the cameras was adjusted in order to obtain a proper field of view. The focusing ring and the aperture were adjusted to achieve clear sparkle images. The cameras were calibrated with regard to position and orientation using a 14 dots × 10 dots grid calibration target plate. The distance of the adjacent dots on the calibration target plate is 4 mm. The cameras were connected to a workstation to collect the images using VIC-Snap software (Correlation Solution Inc.) and the acquisition frequency of the camera was set to two frames per second (fps).

The Instron 5982 electronic universal testing machine was used to load the shear fixture until failure of the shear specimen with a constant loading speed of 0.1 mm/min. The shear stress was calculated as follows:

$$\tau_{xy} = \frac{P}{A} = \frac{P}{lt} \tag{1}$$

where P denotes the applied shear load, A is the minimum cross-sectional area of the specimen, l represents the width across the notches, t is the thickness of the specimen at the notches.
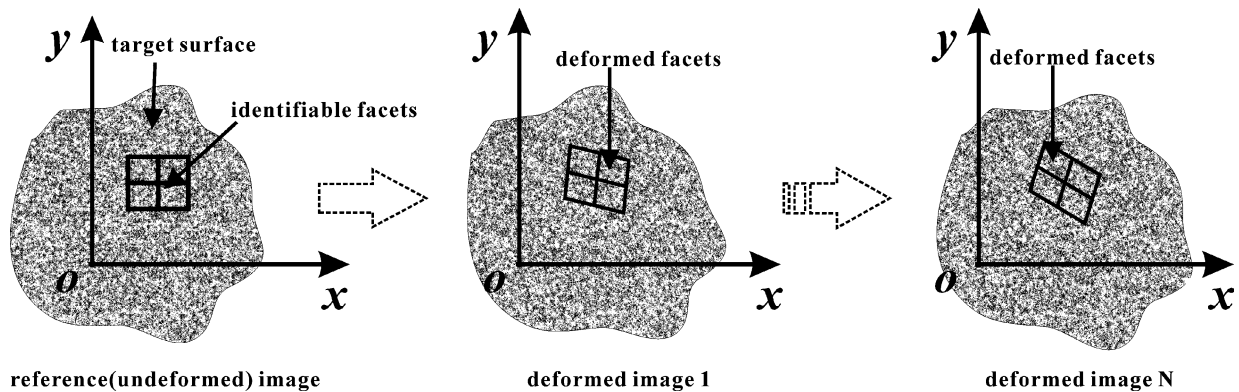

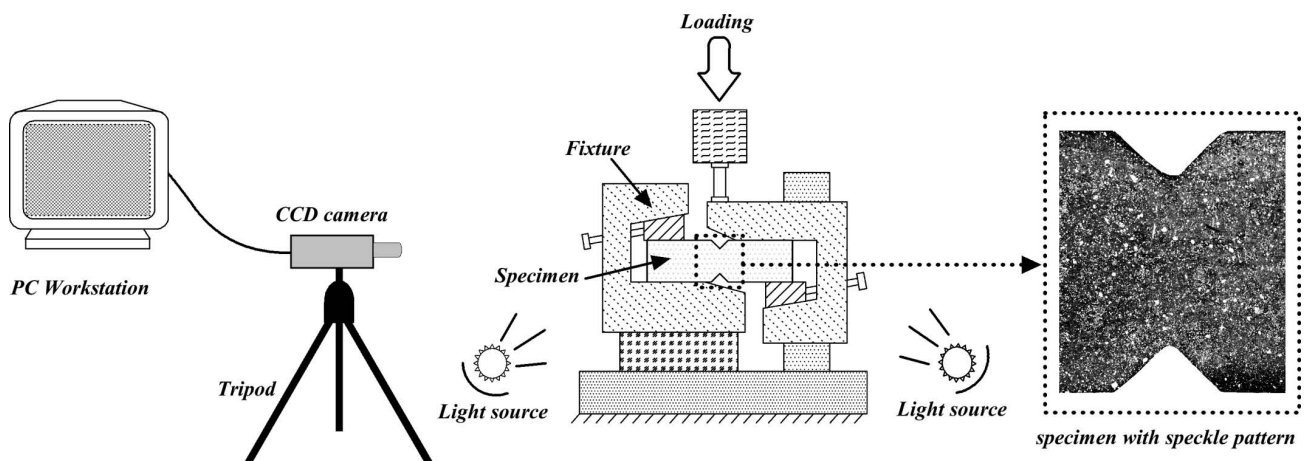**Fig. 3:** Basic schematic diagram of the DIC technique.

Fig. 4: Experimental setup of the DIC testing system.

The VIC-3D software package (Correlation Solution Inc.) was utilized to post-process the collected sparkle images and output the post-processed results. The region around the notches of the shear specimen was selected as the region of interest (ROI). Only the ROI was calculated and post-processed in the VIC-3D software package. The subset size of the ROI was 31 pixels × 31 pixels and the step size was 7 pixels. The displacement and strain field contour of all components can be obtained as long as the post-processing is finished.

III. Results and Discussion

(1) Stress-strain response and shear strain field evolution

The in-plane shear stress-strain response of needled C/SiC composites under monotonic shear loading obtained from the DIC measurement is illustrated in Fig. 5. The response curve shows an initial elastic behavior below stress of ~ 37 MPa (Part I-1 and Part I-2 shown in Fig. 5). With the increase of shear loading, the occurrence and accumulation of shear damage caused the non-linear behavior of the material (Part II shown in Fig. 5). Finally, an apparent plateau region appeared in the curve until failure (Part III shown in Fig. 5).
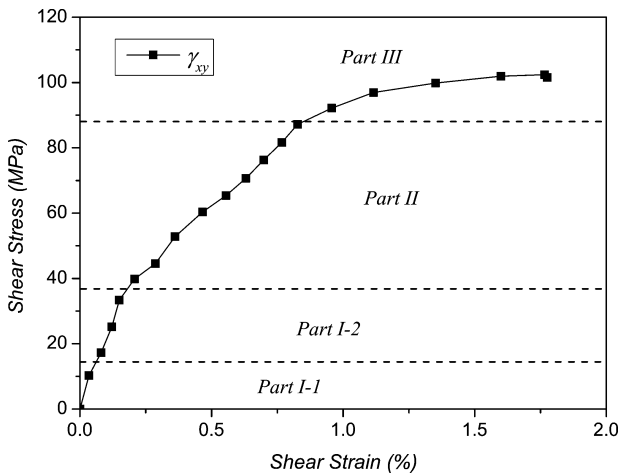

Fig. 5: In-plane shear stress-strain curve of the needled C/SiC composite under monotonic shear loading.

With the purpose of further understanding the non-linear behavior and the shear strain field evolution process of needled C/SiC composites under shear loading, the correlations between the shear stress-strain response and the shear strain field distribution were investigated. According to the strain field patterns, the in-plane shear strain (γ_{xy}) field contour could be divided into four stages. The first stage (see Fig. 6) is below stress of ~ 15 MPa, which corresponds to Part I-1 (see Fig. 5). During this stage, the shear strain field appeared as strain spots, which was mainly caused by the rough surface of the shear specimen. The strain concentration caused by the notches is not obvious. The shear strain contours illustrated here and below were the measuring results of the digital image correlation technique, which were the output data of the VIC-3D software package.
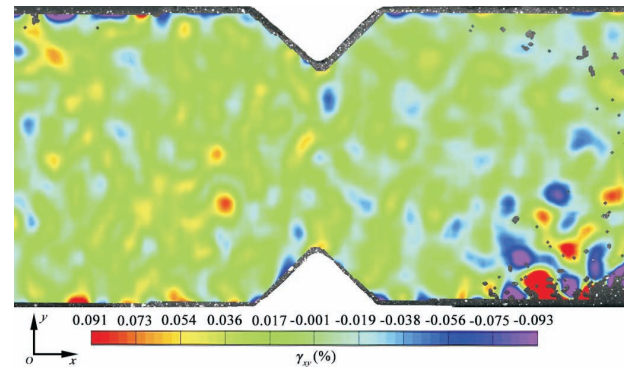

Fig. 6: Shear strain (γ_{xy}) field distribution at a load of 2.86 MPa (Part I-1).

The second stage of shear strain field evolution (see Fig. 7) is between 15 MPa and 37 MPa, which is the formation of shear strain band. During the second stage, the shear strain concentration near the notches became evident (see Fig. 7 a). With the increase of load, the shear strain band between the notches was gradually formed. The second stage corresponds to the Part I-2 illustrated in Fig. 5. Although the shear strain contour was rather non-uniform, the stress-strain curve still remained linear during this stage.
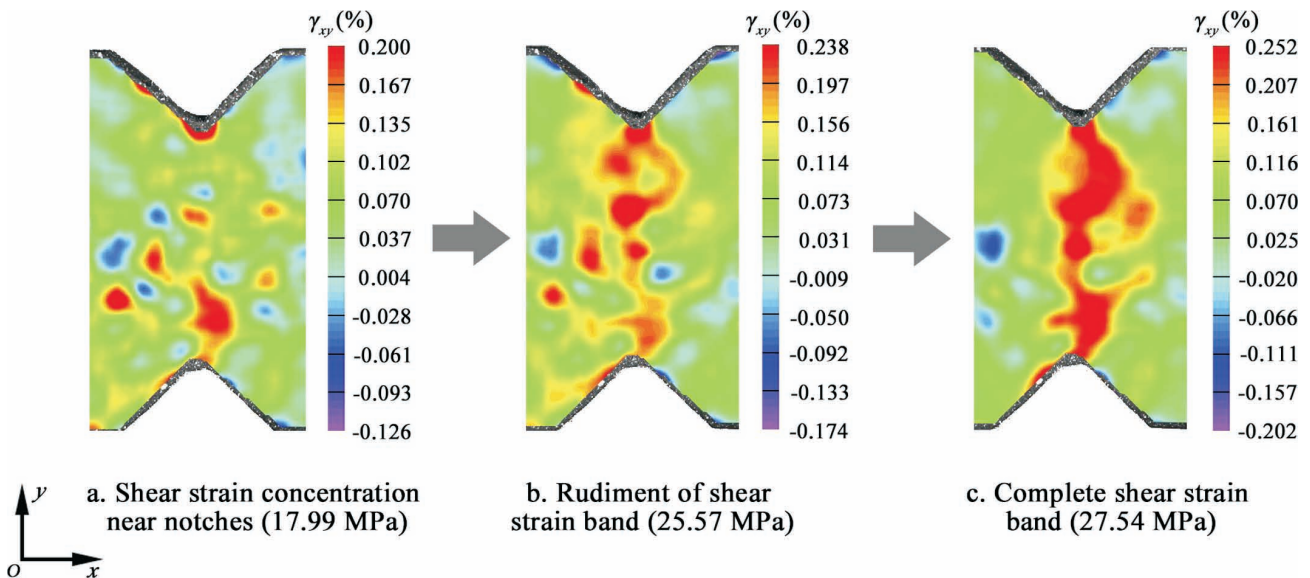

a. Shear strain concentration near notches (17.99 MPa)

b. Rudiment of shear strain band (25.57 MPa)

c. Complete shear strain band (27.54 MPa)

Fig. 7: Formation of shear strain (γ_{xy}) band between the notches of shear specimen (Part I-2).
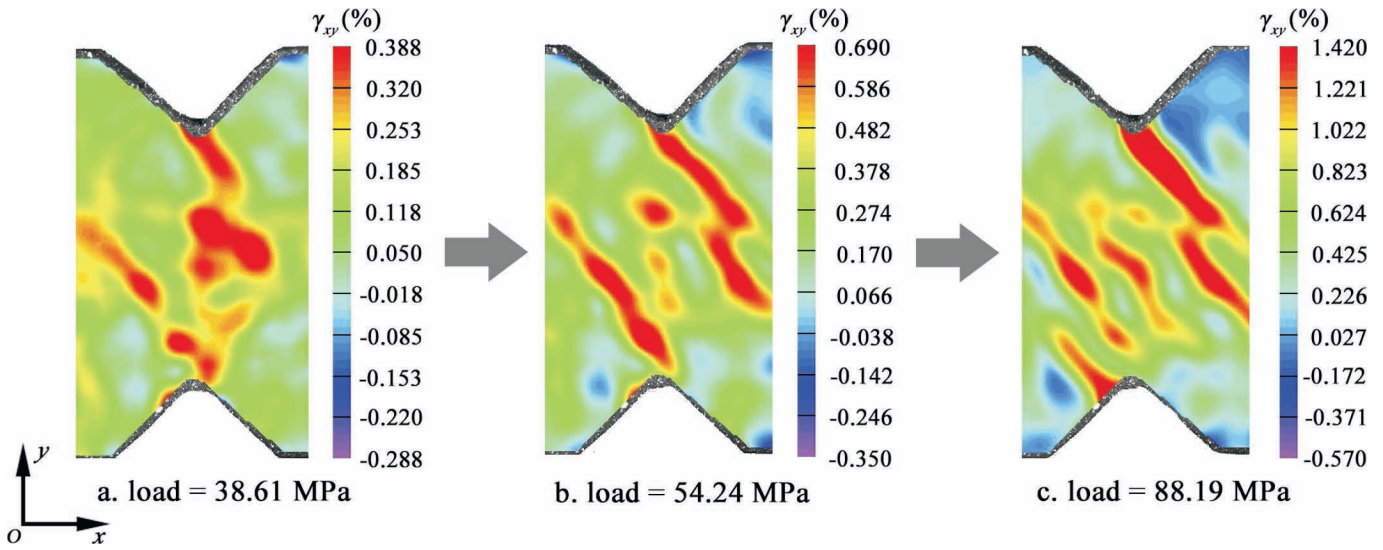
Fig. 8: Formation of slant shear strain (γ_{xy}) bands around the notches of shear specimen (Part II).

The next stage of shear strain field evolution is between 37 MPa and 88 MPa (see Fig. 8). In this stage, the shear strain band between the notches became gradually less prominent and two slant shear strain bands appeared. It can be observed from the captured sparkle images that the location of the two slant shear strain bands and the cracks on the surface of the shear specimen (shown in Fig. 9) overlapped. The contrast and the levels of the shear specimen image were adjusted using Adobe Photoshop in order to highlight the surface cracks. Part II depicted in Fig. 5 corresponds to the third stage of shear strain field evolution. It can be found that the stress-strain response became non-linear during this stage. The secant modulus decreases continuously with the increase of load. The non-linear behavior was partly due to the initiation and propagation of the surface cracks.

The last stage of shear strain field evolution is given in Fig. 10. It can be observed from the shear strain contour that the growth of the surface cracks was the major feature of this stage. The shear strain on the surface cracks increased rapidly. The fast-growing surface cracks led to a rapid decrease of the secant modulus, and a plateau-like region appeared on the shear stress-strain curve (Part III shown in Fig. 5).
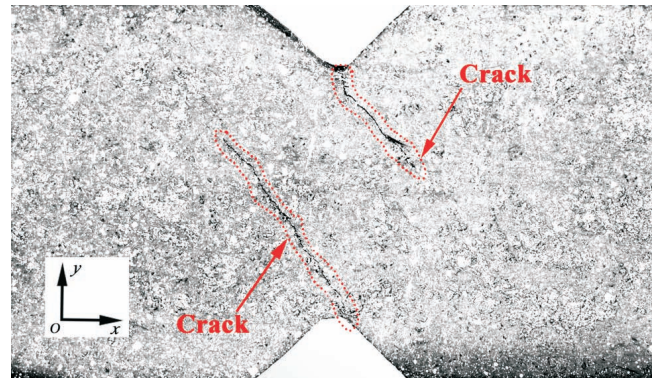

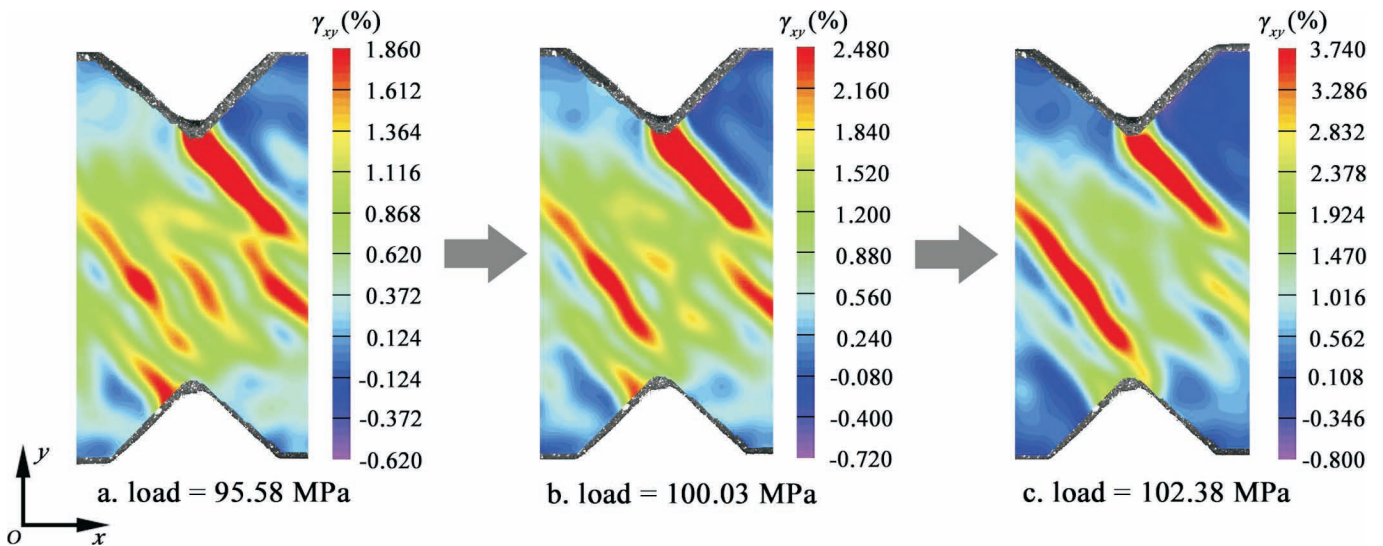**Fig. 9:** Cracks on the surface of the shear specimen.

Fig. 10: Rapid increasing of shear strain (γ_{xy}) on surface cracks (Part III).

The shear stress-strain curves obtained from different-sized calculation areas are collected in Fig. 11. The trends of these stress-strain curves were the same although the calculation areas were quite different. However, the shear stress-strain curves obtained from bigger calculation areas were smoother than those from the smaller ones. This was mainly caused by the inhomogeneous distribution of the shear damage.
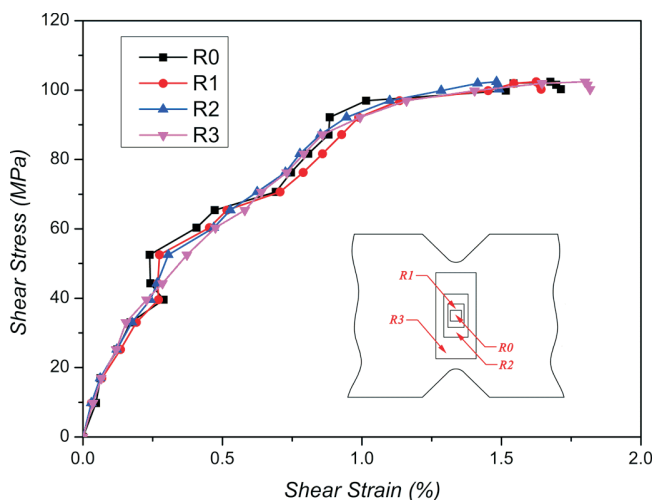

Fig. 11: In-plane shear stress-strain curves of different-sized calculation area.

The shear strain distribution of different percentages of ultimate shear strength (USS) between the notches are plotted in Fig. 12. The shear strain distribution was wave-type, which was far more non-uniform than in the literature [32, 33, 34]. The average distance between the wave peaks (valleys) is about 2.77 mm, which is approximately equal to the average spacing of adjacent needled fiber bundles. Therefore, it can be concluded that the wave-type distributed shear strain between the notches was partly caused by the existence of needled fiber bundles. In addition, it can be found that the value of the wave peaks (valleys) under the same load was different and the location of maximum (minimum) value changed under different loading levels, which reflected the inhomogeneous characteristics of the needled C/SiC composites.

(2) Failure mechanism

The macrofractographies of the needled C/SiC composites' Iosipescu shear specimen can be divided into two types: 1) both upper and lower surfaces exhibit uneven fracture between the notches (see Fig. 13a); 2) one surface of the specimen exhibits uneven fracture between the notches (see Fig. 13a), while another surface of the specimen exhibits oblique fracture (see Fig. 13b). According to the experimental results of this study, delamination will be observed if the macrofractography of the specimen is that shown in Fig. 13b.
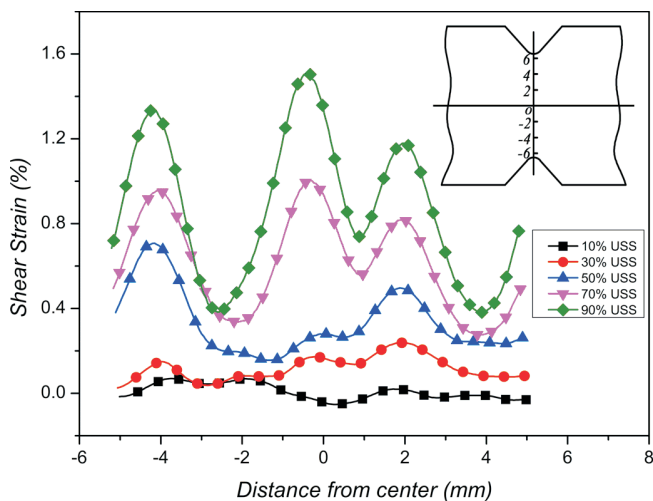

Fig. 12: Shear strain (γ_{xy}) distribution curves of different loading levels along the notches of shear specimen.

a. uneven fracture between the notches	*b. oblique fracture*
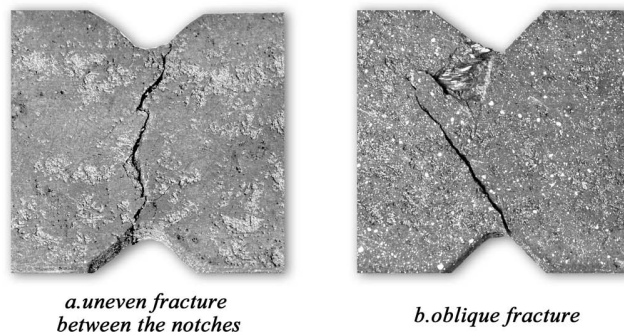
Fig. 13: Two types of shear failure macrofractographies.

It was found that the initiation location of the fractures is not in the middle of the notches but located in the side faces of the notches (see Fig. 13a). The fiber bundles near the notches perpendicular to the loading direction were cut off during the machining process of the shear specimen (Fig. 14). The broken fiber bundles were easier to split than the intact ones. Moreover, the damage extent of fiber bundles in the middle of the notches was smaller than that of the side faces. As a result, the initiation location of the fractures tends to appear on the side faces of the notches rather than in the middle of the notches.
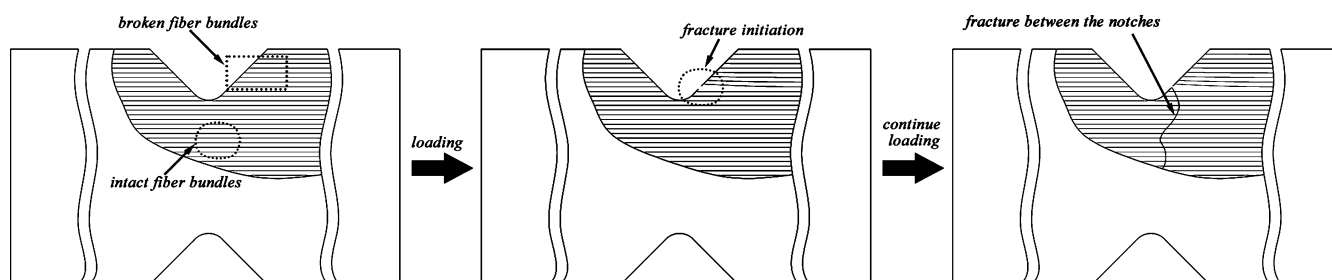

Fig. 14: Diagram of fiber bundle distribution (perpendicular to the loading direction) and fracture evolution around the notches of shear specimen.
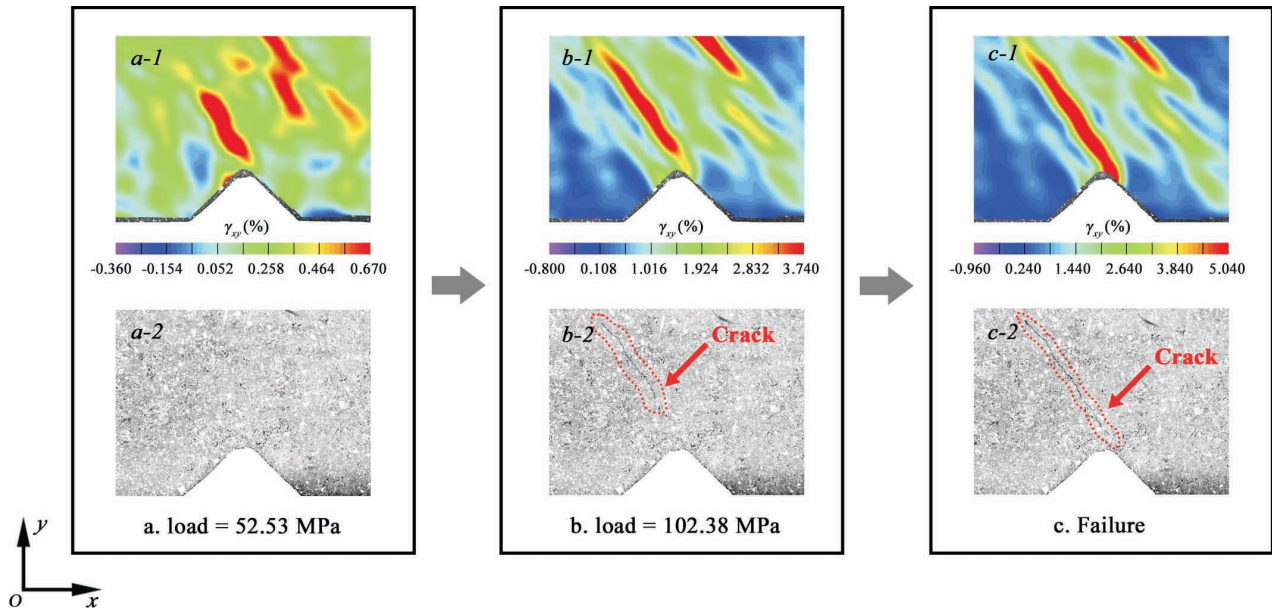
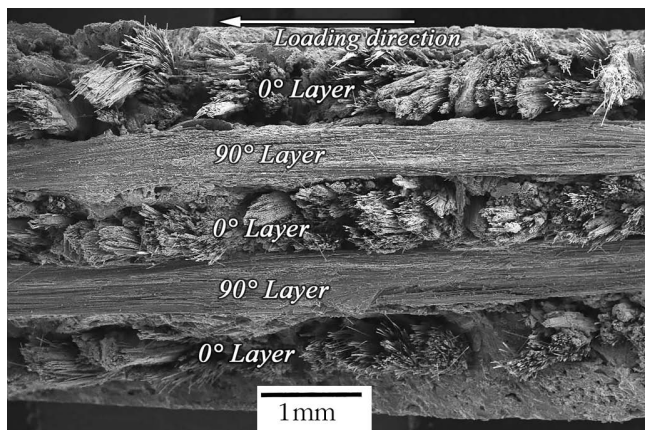**Fig. 15:** Crack initiation and propagation of oblique fracture.

Fig. 16: SEM micrographs of the shear fracture surface.

The shear strain contours and photos of the shear specimen captured during the tests (Fig. 15) shows that the crack of oblique fracture (see Fig. 13b) is not initiated near the notches but in the middle of the specimen. Furthermore, the crack propagated to the notch with the increase of shear load.

The scanning electron microscope (SEM, JSM-6360LV, Japan) was used to take micrographs of the Iosipescu shear specimen. As shown in Fig. 16, the fracture surface of the shear specimen is irregular. It means that the shear failure of needled C/SiC composites was ductile fracture. The fractured fiber bundles of 0° layers (perpendicular to the shear loading) deflected along the direction of the shear load and the end of some fiber bundles were loose after fracture. The 90° layers (parallel to the shear loading) in the fractured surfaces were smoother than 0° layers.

Partial enlarged views of the 0° fiber bundles are shown in Fig. 17. It can be found that the failure mechanisms of 0° fiber bundles under shear loading mainly include matrix cracking (Fig. 17a), fiber fracture (Fig. 17b), debonding of the fiber/matrix interface (Fig. 17b), matrix peeling (Fig. 17c) and fiber pullout (Fig. 17c).

The partial enlarged views of the 90° fiber bundles are shown in Fig. 18. It can be observed that the failure mechanisms of 90° fiber bundles under shear loading mainly include fiber pullout, fiber fracture, matrix peeling, debonding of the fiber/matrix interface and matrix cracking. Extensive relative slipping occurred inside the 90° fiber bundles under shear loading, which led to a mass of matrix peeling on the fracture surface. Moreover, it can be found that the direction of matrix cracking was not perpendicular to the fibers (see Fig. 18a).
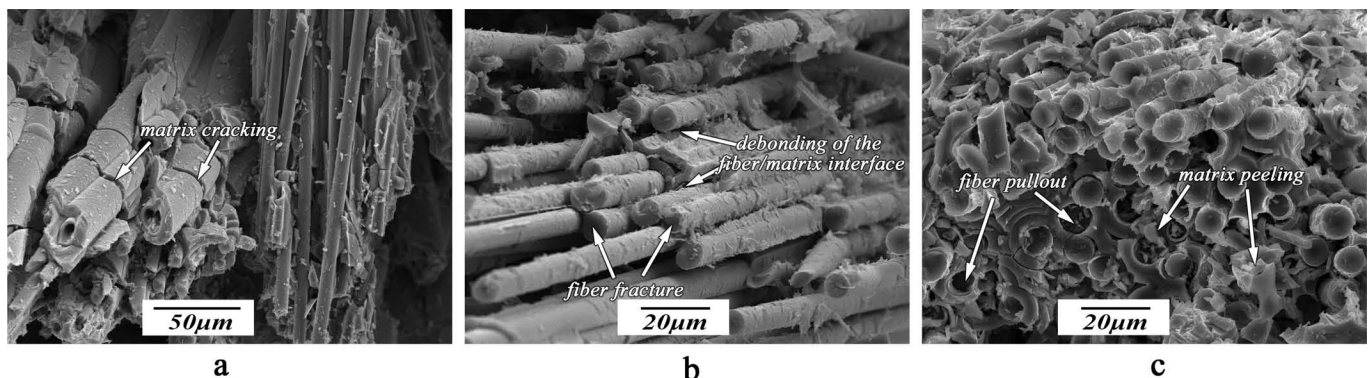

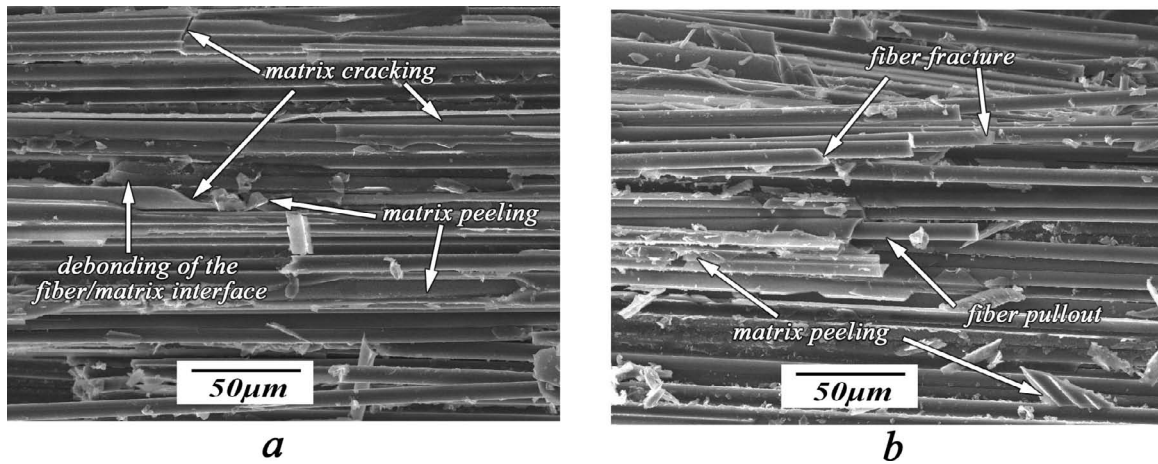**Fig. 17:** SEM micrographs of the failed 0° fiber bundles.

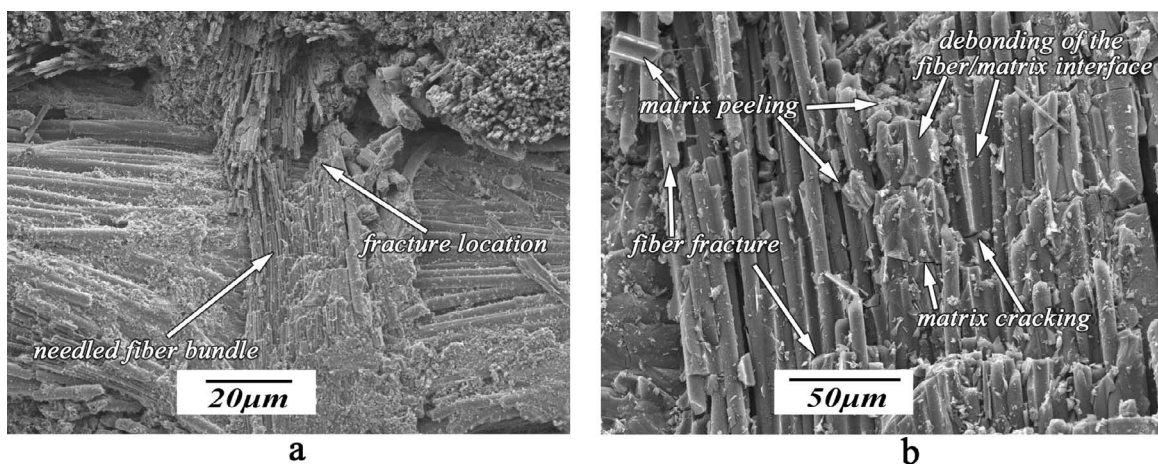**Fig. 18:** SEM micrographs of the failed 90° fiber bundles.

Fig. 19: SEM micrographs of the failed needled fiber bundle: a. overview of the failure location, b. partial enlarged view of the failed needled fiber bundle.

The failure micrographs of needled fiber bundles are given in Fig. 19. It can be observed that the fracture surface of needled fiber bundles was irregular as well (Fig. 19a). The failure mechanisms of fiber fracture, matrix peeling, debonding of the fiber/matrix interface and matrix cracking can be found.

In summary, the failure mechanisms of 90° layer, 0° layer and needled fibers bundle are varied. Matrix cracking, fiber fracture, debonding of the fiber/matrix interface and matrix peeling are the common mechanisms, but the primary failure mechanism of each constituent is different.

IV. Conclusion

The in-plane shear behavior of needled C/SiC composites was investigated with the DIC technique and microscopic observation. Wave-type shear strain distribution between the notches was discovered. The multi-stage shear strain field evolution was analyzed. Special shear failure mechanisms of needled C/SiC composites were found. Major conclusions can be summarized as follows:

(1) The in-plane shear stress-strain response of needled C/SiC composites was non-linear and could be divided into three major parts: initial linear part, non-linear part and plateau part.

(2) The shear strain distribution between the notches was regular wave-type, which reflected the impact of needled fiber bundles on shear strain.

(3) The shear strain field evolution could be divided into four stages. Firstly, the shear strain field distributed as strain spots. Then, the shear strain concentration near the notches was observed and the shear strain band between the notches formed. Subsequently, with the increase of shear load, the shear strain band between the notches became gradually less prominent and slant shear strain bands appeared. Lastly, the shear strain on the surface cracks increased rapidly until failure.

(4) The shear failure of needled C/SiC composites was ductile fracture. Two types of shear fracture could be observed. One was uneven fracture between the notches. The initiation location of the fracture was not in the middle of the notches but located in the side faces of the notches. The other was oblique fracture combined with delamination. The oblique fracture initiated in the middle of the specimen. Matrix cracking, fiber fracture, debonding of the fiber/matrix interface and matrix peeling could be found in 90° layers, 0° layers and needled fibers bundles.

Acknowledgements

References

1   Schmidt, S., Beyer, S., Knabe, H., *et al.*: Advanced ceramic matrix composite materials for current and future propulsion technology applications, *Acta. Astronaut.*, **55**, 409–420, (2004).

2   Misra, A.K., Greenbauer-Seng, L.A.: Aerospace propulsion and power materials and structures research at NASA glenn research center, *J. Aerospace. Eng.*, **26**, 459–490, (2013).

3   Gao, X., Luo, P., Yu, G., *et al.*: Micro-XCT-based finite element method for prediction of elastic modulus of plane woven carbon fiber-reinforced ceramic matrix composites, *J. Compos. Mater.*, **49**, 3373–3385, (2015).

4   Leong, K.H., Ramakrishna, S., Huang, Z.M., *et al.*: The potential of knitting for engineering composites-a review, *Composites Part A*, **31**, 197–220, (2000).

5   Mouritz, A.P., Bannister, M.K., Falzon, P.J., *et al.*: Review of applications for advanced three-dimensional fibre textile composites, *Composites Part A*, **30**, 1445–1461, (1999).

6   Bilisik, K.: Three-dimensional braiding for composites: A review, *Text. Res. J.*, **83**, 1414–1436, (2013).

7   Mouritz, A.P., Leong, K.H., Herszberg, I.: A review of the effect of stitching on the in-plane mechanical properties of fibre-reinforced polymer composites, *Composites Part A*, **28**, 979–991, (1997).

8   Christin, F.A.: Global approach to fiber nD architectures and self-sealing Matrices: from research to production, *Int. J. Appl. Ceram. Tec.*, **2**, 97–104, (2005).

9   Velmurugan, R., Solaimurugan, S.: Improvements in mode I interlaminar fracture toughness and in-plane mechanical properties of stitched glass/polyester composites, *Compos. Sci. Technol.*, **67**, 61–69, (2007).

10 Lacoste, M., Lacombe, A., Joyez, P., *et al.*: Carbon/Carbon extendible nozzles, *Acta. Astronaut.*, **50**, 357–367, (2002).

11 Gautronneau, E., Cros, C., Pascal, P., *et al.*: VEGA Program - The P80 FW SRM Nozzle, Aiaa/asme/sae/asee Joint Propulsion Conference and Exhibit, 2004.

12 Li, Y., Suo, T., Liu, M.: Influence of the strain rate on the mechanical behavior of the 3D needle-punched C/SiC composite, *Mater. Sci. Eng. A*, **507**, 6–12, (2009).

13 Nie, J., Xu, Y., Zhang, L., *et al.*: Microstructure and tensile behavior of multiply needled C/SiC composite fabricated by chemical vapor infiltration, *J. Mater. Process. Tech.*, **209**, 572–576, (2009).

14 Han, C.L., Zhao, D.L., Zhang, L., *et al.*: Microstructure and mechanical property of three-dimensional needled C/SiC composites prepared by precursor pyrolysis, *Key Eng. Mater.*, **434–435**, 45–47, (2010).

15 Mei, H., Li, H., Bai, Q., *et al.*: Increasing the strength and toughness of a carbon fiber/silicon carbide composite by heat treatment, *Carbon.*, **54**, 42–47, (2013).

16 Xu, H., Zhang, L., Cheng, L.: The yarn size dependence of tensile and in-plane shear properties of three-dimensional needled textile reinforced ceramic matrix composites, *Mater. Des.*, **67**, 428–435, (2015).

17 Fang, G., Gao, X., Yu, G., *et al.*: Effect of the stress level on the fatigue strengthening behavior of 2D needled C/SiC CMCs at room temperature, *Mater. Des.*, **89**, 432–438, (2016).

18 Choi, S.R., Bansal, N.P., Gyekenyesi, J.P.: Dependency of shear strength on test rate in SiC/BSAS ceramic matrix composite at elevated temperature, NASA TM-2003-212182 2003.

19 Yan, K.F., Zhang, C.Y., Qiao, S.R., *et al.*: Failure and strength of 2D-C/SiC composite under in-plane shear loading at elevated temperatures, *Mater. Des.*, **32**, 3504–3508, (2011).

20 Naslain, R.: Design, preparation and properties of non-oxide CMCs for application in engines and nuclear reactors: an overview, *Compos. Sci. Technol.*, **64**, 155–170, (2004).

21 Tang, S.F., Deng, J.Y., Du, H.F., *et al.*: Fabrication and microstructure of C/SiC composites using a novel heaterless chemical vapor infiltration technique, *J. Am. Ceram. Soc.*, **88**, [11], 3253–3255, (2005).

22 Tang, S.F., Deng, J.Y., Wang, S.J., *et al.*: Fabrication and characterization of C/SiC composites with large thickness, high density and near-stoichiometric matrix by heaterless chemical vapor infiltration, *Mat. Sci. Eng. A*, **465**, 1–7, (2007).

23 ASTM D5379/D5379M-12:2012. Standard test method for shear properties of composite materials by the V-Notched Beam Method.

24 Sutton, M.A., Wolters, W.J., Peters, W.H.I., *et al.*: Determination of displacements using an improved digital image correlation method, *Image. Vision. Comput.*, **1**, 133–139, (1983).

25 Chu, T.C., Ranson, W.F., Sutton, M.A.: Applications of digital-image-correlation techniques to experimental mechanics, *Exp. Mech.*, **9**, 1981–1993, (2009).

26 Bruck, H.A., Mcneill, S.R., Sutton, M.A., *et al.*: Digital image correlation using newton-raphson method of partial differential correction, *Exp. Mech.*, **29**, 261–267, (1989).

27 Grediac, M.: The use of full-field measurement methods in composite material characterization: interest and limitations, *Composites Part A*, **35**, 751–761, (2004).

28 Makeev, A., He, Y., Carpentier, P., *et al.*: A method for measurement of multiple constitutive properties for composite materials, *Composites Part A*, **43**, 2199–2210, (2012).

29 Sutton, M.A., Orteu, J.J., Schreier, H.: Image correlation for shape, motion and deformation measurements: basic concepts, theory and applications. Springer Science & Business Media, 2009.

30 Kashfuddoja, M., Ramji, M.: Whole-field strain analysis and damage assessment of adhesively bonded patch repair of CFRP laminates using 3D-DIC and FEA, *Composites Part B*, **53**, 46–61, (2013).

31 Toubal, L., Karama, M., Lorrain, B.: Stress concentration in a circular hole in composite plate, *Compos. Struct.*, **68**, [1], 31–36, (2005).

32 Mistou, S., Fazzini, M., Karama, M.: Shear test on CFRP full-field measurement and finite element analysis, *Adv. Mater. Res.*, **112**, 49–62, (2010).

33 Johnson, W.S., Masters, J.E., Wilson, D.W., *et al.*: Evaluation of four composite shear test methods by digital speckle strain mapping and fractographic analysis, *J. Compos. Tech. Res.*, **22**, 161–172, (2000).

34 Melin, L.N., Neumeister, J.M.: Measuring constitutive shear behavior of orthotropic composites and evaluation of the modified iosipescu test, *Compos. Struct.*, **76**, 106–115, (2006).